Structural studies of epitaxial ultrathin oxide films and nanoclusters by means of angle-scanned photoelectron diffraction (XPD)

2002 J. Phys.: Condens. Matter 14 4101

(http://iopscience.iop.org/0953-8984/14/16/304)

INSTITUTE OF PHYSICS PUBLISHING JOURNAL OF PHYSICS: CONDENSED MATTER

J. Phys.: Condens. Matter **14** (2002) 4101–4117 PII: S0953-8984(02)29077-3

Structural studies of epitaxial ultrathin oxide films and nanoclusters by means of angle-scanned photoelectron diffraction (XPD)

Gaetano Granozzi[1], **G Andrea Rizzi and Mauro Sambi**

Dipartimento di Chimica Inorganica, Metallorganica ed Analitica e Unità INFM, Università di Padova, via Loredan 4, 35131 Padova, Italy

E-mail: granozzi@unipd.it

Received 25 September 2001
Published 11 April 2002
Online at stacks.iop.org/JPhysCM/14/4101

Abstract

Selected examples of the application of angle-scanned x-ray photoelectron diffraction (XPD) to structural studies of epitaxial oxide ultrathin films and nanoclusters deposited either on metal or on oxide single-crystalline substrates are briefly reviewed. A short introduction discusses the preparative strategies adopted in order to grow the desired oxide systems, as well as the basic features of the XPD technique which are relevant to the field of oxide epitaxy. Synthesis routes include both e-beam metal evaporation and oxidation and a modification of metal–organic chemical vapour deposition to suit ultra-high-vacuum conditions. These introductory remarks are followed by an overview of some systems that have been investigated in our laboratory. The discussion is particularly aimed at highlighting the peculiar capabilities and strengths of photoelectron diffraction applied to—even short-range-ordered—oxide epitaxial systems. Oxide overlayers obtained by means of reactive deposition or post-oxidation comprise various vanadium oxide phases grown on rutile $TiO_2(110)$, while metalcarbonyl precursor decomposition in an oxygen atmosphere as a source of oxide ultrathin films is illustrated through the cases of $RuO_2/TiO_2(110)$ from $Ru_3(CO)_{12}$ and MnO/Pt(111) from $Mn_2(CO)_{10}$. Finally, some remarks are made on recent developments and future perspectives in the field of synchrotron-radiation-based implementations of photoelectron diffraction and holography.

(Some figures in this article are in colour only in the electronic version)

1. Introduction

Oxide-based inorganic materials are nowadays of paramount technological relevance. The basic reasons for this strong interest of applied character lie in the extreme variety and versatility of oxides, as well as in the possibility of integrating their functionalities in electronic

[1] Corresponding author.

devices [1, 2]. As a matter of fact, oxides display electric conductivities which range from those typical of dielectrics to those of superconductors (spanning approximately ten orders of magnitude) and peculiar optical (from photorefractivity to optical nonlinearity), magnetic and ferroelectric properties. Moreover, oxides have an essential role in the field of heterogeneous catalysis, either as the active catalytic species or as supports for the actual catalysts, and the technology of gas-sensing devices is largely based on oxides. In addition, their ionic conduction properties are heavily exploited in the technology of solid-state storage batteries and oxide thin films are used as corrosion-resistant coatings and as thermal barriers. Since a great many of the mentioned applications stem from the surface properties of oxide materials, the surface science of oxides has acquired an ever-growing importance in the last decade, as testified by the continuous increase in the number of oxide-related publications in the literature.

Despite this applied interest, there are still some open questions concerning oxide surfaces at a fundamental level on such topics as the surface atomic structure, the electronic properties, the forces governing surface reactivity and the role played by defects [3]. Besides the intrinsic difficulties related to the complexity of oxide systems, there are some additional obstacles that explain the lack of detailed information on oxide surfaces, the most important being (i) the lack of good quality surfaces and (ii) the insulating nature of many oxide-based materials. These drawbacks have made the application of many ultra-high-vacuum (UHV) techniques based on charged probe-particles (electrons, ions, ...) difficult.

When these materials are present as ultrathin films (with a maximum thickness of approximately a few nanometres), they gain further interest because innovative properties with respect to bulk phases, which arise from the interaction with the substrate and/or from the confinement to atomic-scale structures in at least one dimension, can be exploited. Indeed, the innovation with ultrathin films is associated with the possibility of stabilizing phases and structures which are not obtainable in bulk form due to thermodynamic and/or kinetic constraints. Moreover, an effective way of overcoming charging problems in insulating materials is to resort to ultrathin layers in order to prepare model oxide surfaces [4]. Actually, if the substrate is a good conductor (e.g. a metal or another conductive oxide), the reduced thickness of the oxide overlayer allows the charged probe-particles to tunnel toward the substrate. This approach has provided ordered oxide surfaces viable for STM, photoemission and electronic excitation investigations.

The interactions at the interface between the substrate and the ultrathin film give rise to the above-discussed phenomena: in order to optimize such interactions, in many cases the film adjusts its structure to that of the substrate, producing a strain which is maintained until a critical thickness is reached, over which it recovers its thermodynamically more stable bulk structure. Hence, most of the innovative character associated with ultrathin films is connected to the first few atomic layers, which are composed by atoms placed in unusual positions and characterized by electronic interactions which are different from those present in the bulk phase.

Our research interest in the last few years has been mainly focused toward innovative routes for preparing ultrathin ordered oxide films in UHV conditions having specific compositional and/or structural and morphological peculiarities. To reach this goal, the use of angle-scanned x-ray photoelectron diffraction (XPD) as an *in situ* structural probe was revealed to be extremely useful. Actually, XPD can provide information on the nature of the growth easily and directly from the XPD data (on such issues as the epitaxial character of the overlayer/substrate interface, the detailed epitaxial relationships with the substrate and the presence and the magnitude of interlayer expansions or contractions). More complete structural information is accessible via a trial-and-error procedure using multiple-scattering-based theoretical simulations of the XPD patterns.

In the present short review, after a qualitative discussion of preparative issues and of the main features of the XPD technique relevant to our subject matter (excellent reviews on XPD are available in the literature [5–12]), we report some selected results in the field of ultrathin epitaxial oxide films obtained in our laboratory during the last few years. At the end we also briefly comment on the future trends and perspectives.

2. Methodology

2.1. Preparative strategies

Since the film deposition is typically under kinetic control, the results in terms of structure and properties are strongly dependent on the preparative route that has been followed. This general consideration led us to explore rather different preparative approaches. The first two of them, referred to as post-oxidation (PO) and reactive deposition (RD), originate from standard metal deposition on the substrate, where the oxidative step is undertaken either during the deposition (RD) or after the metal particle nucleation (PO). The choice of the oxidant is rather important in order to determine the final product and a little chemical intuition is strongly recommended in this sense.

The third route we have been exploring is related to the use of volatile metalcarbonyl precursors which are thermally decomposed on the substrate surface. This route may give an alternative way to deposit metal particles or it could lead to products of a different nature, depending on the presence of other reactants. Actually, in the presence of an oxidant, ultrathin oxide films can be easily prepared. This topic is connected to and derived from the well known MO-CVD (metal–organic chemical vapour deposition) [13] growth technique. While the latter is usually carried out at reduced pressures and leads to layers up to several micrometres thick, in our context only the initial stages of epitaxy in UHV are involved and ultrathin films are consequently grown. One of the appealing features of this route is related to the possibility that the surface reaction limits the deposition step to a well selected thickness of the overlayer. This may happen when the chemical nature of the substrate is not irrelevant with respect to the whole process, leading to self-limiting growth mechanisms. (e.g. the growth stops when the substrate is completely covered by the ultrathin film). Moreover, when using polymetallic metalcarbonyls (see below), the possible preservation of the metallic cage during the nucleation step could imply new perspectives with respect to the structure and morphology of the final product. Metalcarbonyls are usually characterized by high vapour pressures and good stability at room temperature and they can be easily purified by sublimation or re-crystallization. In our case the metalcarbonyl precursors are introduced into the UHV preparation chamber through a doser, which consists of a perforated tantalum foil pocket mounted inside a UHV stainless steel tube and held in place with threaded rods. The doser is isolated from the main analysis chamber by a gate valve and can be evacuated independently, thus avoiding significant contamination of the UHV system. The decomposition mechanism of metalcarbonyls always implies the interaction with the heated substrate surface with an initial formation of sub-carbonyl species followed by a complete decarbonylation and formation of metal particles. The chemical interaction between the carbon monoxide, the substrate and the metal to which it is bound plays a crucial role in determining the growth mechanism, which implies adsorption and decomposition on the surface and can often lead to a cluster-like growth of metals or oxides. Thus, the use of metalcarbonyls as alternative sources for metal or oxide deposition opens the interesting possibility of depositing nanoclusters. XPD is probably the only surface science tool able to characterize with chemical specificity the growth of short-range-ordered metal or oxide nanoclusters.

2.2. XPD in situ structural characterization

The ambitious task of optimizing the deposition parameters to obtain a specific product would be unattainable without resorting to an efficient *in situ* structural tool to analyse the deposits. To this end XPD was revealed to be of strategic relevance. In the following we will briefly discuss some major feature of XPD.

Photolectrons and Auger electrons emitted from the surface region of a crystalline sample under x-ray irradiation undergo scattering by atoms in the vicinity of the emitting species. Subsequent interference between the primary and the scattered electron waves (originated by the scattering of the primary wavefront at atoms surrounding the emitter) produces intensity modulations as a function of either the direction of detection or the kinetic energy (KE) of the emitted electron, giving rise to angle-scanned XPD (usually indicated as XPD) [5–8] and energy-scanned PD (also known as angle-resolved photoemission fine structure, ARPEFS) [14], respectively. The resulting modulations, properly interpreted, are rich in structural information relative to the near-surface atomic layers. Most of our work is based on angle-scanned XPD, although ARPEFS measurements have been occasionally performed as well [15].

PD is a surface structural probe sensitive to short-range order, with atomic, chemical state and site specificity. The short-range order sensitivity is due to the lack of coherence between photoelectron waves emitted at different atomic sites because of the random nature of the emission process [9], coupled with the relatively short electron inelastic mean free paths at the energies typical for a PD experiment. The atomic and chemical state specificity stem from the features of conventional x-ray photoelectron spectroscopy (XPS). In fact, XPD patterns are obtained experimentally simply by singling out a spectral feature from an XPS spectrum of an (at least locally) ordered sample, and by monitoring its intensity as a function of the emission direction. Angle-scanned experiments are usually carried out by moving the sample on a suitable manipulator which allows the sweeping of the emission direction over the full hemisphere above the sample surface [16]. Intensity maps are then reported as 2π stereographic projections, where a radial cut from the plot centre to the outer diameter represents a polar (θ) scan from the sample normal to grazing emission, while a circular cut at fixed θ represents an azimuthal (ϕ) scan. Photoemission intensity is given by the colour scale. The anisotropy χ, defined as $\chi = (I_{\max} - I_{\min}) \times 100/I_{\max}$, can be as high as 70% on well ordered crystalline samples. XPD patterns can therefore be obtained for different core levels of the same element, of various elements present on the surface, and, at higher energy resolution, even of different chemical states of the same element.

One of the strongest features of XPD in the 400–1500 eV energy regime is the dominance of forward-scattering (FS) [6] in the electron–atom scattering process. As a consequence, polar and/or azimuthal scans for sufficiently energetic electrons furnish the information on bond orientations directly, since in this energy regime the intensity is enhanced when the angle between the emitter–scatterer and the emitter–detector directions is close to 0°, i.e. whenever a scatterer intersects the emitter–detector direction. This zeroth-order interference effect is a very effective tool for the determination of internuclear directions and it has been successfully exploited for the determination of the growth mode and of interlayer contractions or expansions of strained overlayers in studies of epitaxial growth [10, 11].

On the other hand, the information on bondlengths is contained in the first-order and higher-order interference fringes, associated with scattering angles higher than 0°. In order to exploit all the structural information present in an XPD pattern, the most fruitful approach relies on trial-and-error fitting of the experimental data to theoretical simulations of the XPD plots, carried out assuming a structural model for the system under investigation—usually a cluster

containing from some tens to some hundreds of atoms [16]. Emitted intensities as a function of the emission direction are calculated by propagating electrons (treated as curved wavefronts) within the cluster, in the framework of either a single-scattering or a multiple-scattering model, leading to the SSC–SW (single-scattering–spherical-wave) or MSC–SW (multiple-scattering–spherical-wave) approaches, respectively [6]. In the last few years, simulations at the MS level have been efficiently performed by means of the MSCD code by Chen and Van Hove [17]. SS does well at high photoelectron KE, except for an overestimation of FS intensities, while MS is more appropriate for lower KE, and in general for an overall better simulation of relative intensities. Sets of simulated data are obtained as a function of the structural parameters to be optimized, and the best-fit structure is usually obtained through an R-factor analysis [18–22].

In the following section, selected experimental results in the field both of e-beam evaporation and of metallocarbonyl precursor decomposition will be reported, with a particular emphasis given to the nature and degree of detail of structural information that can be pursued through the use of XPD.

3. Results

3.1. Vanadium oxides on TiO_2(110)

3.1.1. Submonolayer coverages: vanadia nucleation sites at the TiO_2(110) surface [23]. Vanadium oxides dispersed on titania (TiO_2) represent a very attractive research subject because they display catalytic activity in many hydrocarbon partial oxidation reactions [24, 25] and in nitric oxide selective reduction reactions [26]. It has been demonstrated that the substrate not only increases the catalyst surface area, but also influences its activity and selectivity. Model systems such as metallic vanadium and vanadium oxide thin films on single-crystalline TiO_2—studied by means of the surface science techniques which are capable of providing both structural and chemical information—could be precious in explaining the basic mechanisms through which the particular activity and selectivity of titania-supported vanadium oxides are established. For this reason, we have devoted much attention to this subject in recent years [23, 27–33].

One of our first works in the field [28] was devoted to the stepwise deposition of metallic vanadium on TiO_2(110), each step being followed by PO at 150 °C in 2×10^{-6} mbar of O_2. We were able to demonstrate that the obtained overlayer was rutile VO_2(110), pseudomorphic to the substrate, with well developed long- and short-range order. This investigation was preceded by a chemical and structural investigation of the initial stages of epitaxy, when small amounts of vanadium (in the sub-ML range) are deposited on TiO_2(110), in order to check which nucleation site is responsible for the epitaxial ordering of the epilayer [23]. For this purpose, an interface was prepared by depositing 0.2–0.3 ML of vanadium at room temperature on the TiO_2(110) surface. The chemical nature of the deposit was investigated by means of XPS measurements, while the local structure of vanadium atoms was checked by means of XPD. The chemical and structural characterization was repeated after a short annealing at 473 K in UHV conditions. The as-deposited layer shows a strong attenuation of the initially sharp (1×1) LEED pattern of the clean and stoichiometric rutile substrate, indicative of a substantial increase of surface disorder upon deposition, while XPS demonstrates that a surface reaction is taking place accompanied by a V $\rightarrow$ Ti charge transfer: V is partially oxidized. If a short annealing at 473 K at a pressure of 10^{-10} mbar is performed, XPS shows that the Ti 2p line returns to the fully symmetric shape typical of stoichiometric TiO_2(110) and the (1×1) LEED pattern recovers its initial sharpness, while V is further oxidized with respect to the as-deposited layer. If XPD is now applied to the V 2p photoemission line from the

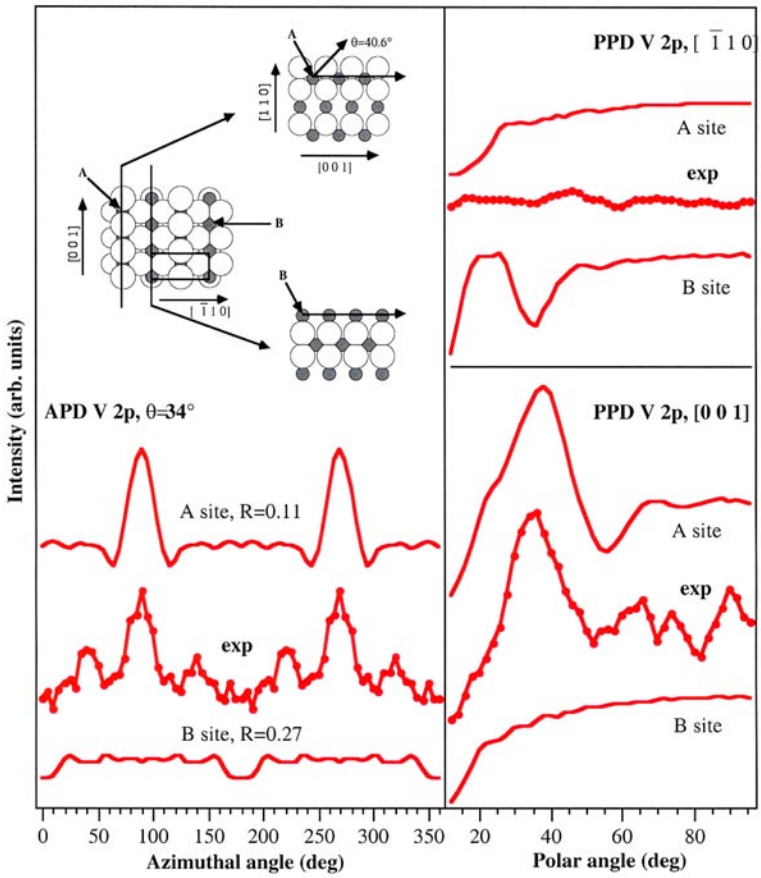

Figure 1. Left: experimental V $2p_{3/2}$ XPD azimuthal scan at the polar angle $\theta = 34^\circ$ for 0.2 ML of V deposited at the TiO_2(110) surface and annealed at 473 K for 1 min compared with SSC–SW simulations assuming either A or B substitutional sites for V atoms in the first TiO_2 layer. *R*-factors are quoted. The inset shows the top view and two non-equivalent cuts normal to the surface plane along the [001] azimuth for the (1 × 1) TiO_2 (110) surface. Sixfold-coordinated (A) and fivefold-coordinated (B) Ti cationic sites are highlighted. The cation → anion FS along the [001] azimuth at $\theta = 40.6^\circ$ for a bulk-terminated surface is indicated. Right: experimental V $2p_{3/2}$ XPD polar scans along the [$\bar{1}$10] (top) and the [001] (bottom) main azimuths for the 0.2 ML V deposit compared with SSC–SW simulations assuming either A or B substitutional sites for V atoms in the topmost substrate layer.

sub-monolayer V coverage, it is possible to demonstrate that V atoms occupy selected surface sites on the TiO_2(110) substrate. For this purpose, a V 2p XPD azimuthal scan has been run at $\theta = 34^\circ$ from the surface for the annealed layer: a clearly twofold symmetric curve is obtained (figure 1), with an anisotropy as high as 24%, and two intensity maxima at $\phi = 90^\circ$ and 270° are clearly seen, corresponding to the [001] and [00$\bar{1}$] main azimuths of the substrate (see the model reported in figure 1). The presence of strong intensity modulations of the V 2p signal means that V atoms occupy selected and equivalent sites on the titania surface. If the two intensity maxima at 180° from each other, which reflect the twofold symmetry of the substrate, are tentatively assigned to FS events, it may be thought that V sites are of the substitutional type, possibly in the first atomic layer of the substrate. In order to confirm this guess, SSC–SW simulations have been performed by putting V atoms in either A (sixfold-coordinated) or

B (fivefold-coordinated) cationic sites on the $TiO_2(110)$ surface (see the model in figure 1). Agreement is clearly superior for A-site occupation, and this conclusion is also corroborated by the comparison of experimental and simulated polar scans along the main substrate azimuths (figure 1): a peak is found along the short side of the unit cell (i.e. the [001] azimuth) at the polar angle $\theta = 34^\circ$, which corresponds to the sixfold-coordinated V $\rightarrow$ bridging O FS, while no peak is found along the long side of the unit cell, which is indeed expected if no V atoms are present in B surface sites (if it were not so, a FS peak at $\theta \sim 20^\circ$ would be detected along this azimuth due to fivefold-coordinated V $\rightarrow$ bridging O FS, as clearly seen in the top right panel of figure 1). In addition, surface-terminating bridging oxygen atoms bonded to sixfold-coordinated V atoms are found to relax downward by approximately 0.2 Å, judging from the shift of V $\rightarrow$ O FS polar angle from the bulk-expected $\theta = 40^\circ$ to the experimentally found $\theta = 34^\circ$. Simulations are also consistent with V atoms present exclusively in the topmost surface layer—V atoms in sub-surface layers would in fact produce additional peaks which are not detected in experimental scans.

3.1.2. Short-range-ordered epitaxial layers of VO on $TiO_2(110)$ [30, 31]. If the PO treatments following V deposition steps are performed by annealing the sample in UHV rather than in an oxygen atmosphere, instead of producing long-range-ordered epitaxial VO_2, we rather obtain a short-range-ordered oxide whose V $2p_{3/2}$ feature stabilizes at 513.5 ± 0.1 eV, a value between that of metallic vanadium and V_2O_3 [30]. The oxidation of the deposited metal is achieved through bulk-to-surface oxygen diffusion during the annealing treatments. If a complete 2π XPD characterization of a 5 ML thick layer is performed [31], we notice (figures 2(*a*) and (*c*)) that the V 2p and O 1s 2π plots are very similar to each other as far as the main peak positions and intensities are concerned. The observation of analogous XPD modulations for two different species is strongly indicative of an analogous structural environment experienced by both of them. Coupled to the information given by the V 2p XPS binding energy, there is quite good evidence for the fact that the ultrathin film has a composition close to VO and a rock-salt structure, which implies that both ions experience the same sixfold coordination due to near-neighbouring counterions. (In bulk VO_x, the cubic lattice structure is maintained for $0.8 \leqslant x \leqslant 1.3$.) The structure is confirmed by MSC–SW calculations, whose best-fit results are reported in figures 2(*b*) and (*d*) for V 2p and O 1s emission, respectively. The best fit corresponds to a VO(100)/TiO_2(110) orthorhombically strained epitaxial matching of the overlayer to the substrate (see figure 2(*e*)). The epitaxial strain of the cubic NaCl-like VO lattice implies a 7% expansion of the lattice parameter along the [010] and [001] overlayer directions and a reduction of the angle between the two unit vectors from 90° to 84.6°, along with a substantial interlayer contraction by as much as 16%, although the simulations appear to be rather insensitive to this parameter, which can be decreased down to 12% without a substantial increase of the *R*-factor. A further improvement of the fit is obtained if a buckling of 0.5 ± 0.1 Å is introduced in the overlayer along its [011] direction (corresponding to the $[\bar{1}10]$ direction of the substrate), as shown schematically in figure 2(*f*). Buckling along this direction is needed to match the overlayer unit cells to the protruding rows of bridging oxygen atoms found at the $TiO_2(110)$ surface.

For this particular vanadia phase on $TiO_2(110)$, grown by matching the metal deposition rate to the oxygen diffusion kinetics from the bulk, it has been found that small modifications of the deposition rate and annealing temperature can yield non-stoichiometric oxides, with an oxidation state only slightly higher than metallic vanadium, or compounds with a too high oxidation state, such as V_2O_3 (but see section 3.1.3) or even defective VO_2. For this reason, XPD has proven once more to be of paramount importance for its capability of monitoring *in situ* the structure of the grown layers, in order to relate it reliably to the growth conditions which have been employed.

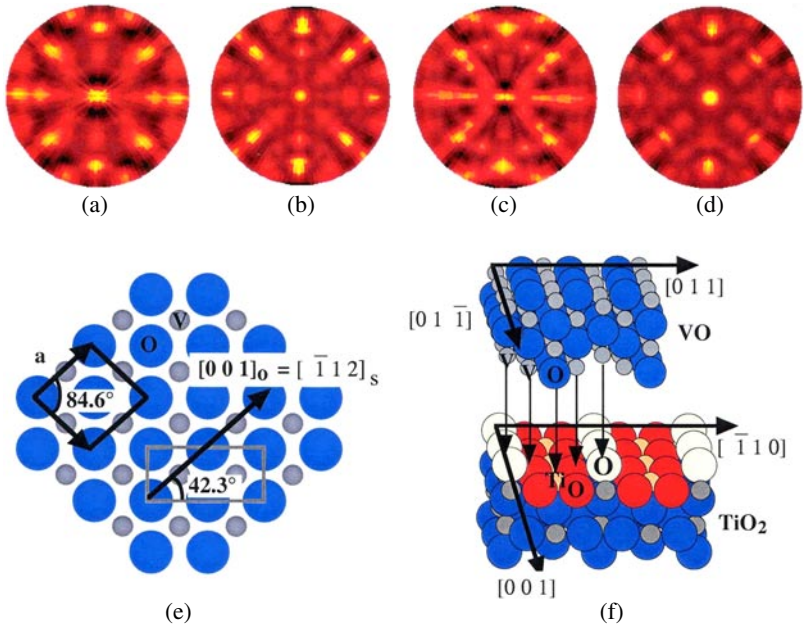

Figure 2. Experimental and simulated (MS) 2π plots for V 2p ((*a*) and (*b*), respectively), and O 1s ((*c*) and (*d*), respectively) from a 4 ML thick VO overlayer deposited on the $TiO_2(110)$ surface. (*e*) Top view of a strained single monolayer of VO(100) pseudomorphic to $TiO_2(110)$. A strained centred overlayer unit cell with lattice parameter $\boldsymbol{a}$ is shown (left). The substrate unit cell is highlighted as a grey rectangle (right). The matching of the overlayer [001] direction to the substrate [$\bar{1}$12] azimuth is shown. (*f*) Matching of VO(100) to $TiO_2(110)$. Surface bridging oxygen atoms of the substrate are shown as white circles. The main azimuthal directions on both the overlayer and the substrate are indicated. The buckling of the overlayer along its [011] azimuth is shown.

3.1.3. Vanadia RD on $TiO_2(110)$ in oxygen [32]. Electronic structure data collected on vanadia deposited either on titania or on other single-crystal surfaces (such as alumina and several noble metals) seem to demonstrate that the RD procedure in an oxygen ambient leads invariably to overlayers of V_2O_3, no matter what the substrate. This conclusion is based on x-ray photoelectron spectroscopy (XPS), x-ray excited Auger electron spectroscopy (XAES) and near-edge x-ray absorption fine-structure (NEXAFS) measurements [34, 35], which are in good agreement with features expected for bulk V_2O_3 and do not vary appreciably if the substrate is changed. However, little was known up to now regarding the detailed atomic structure of the overlayers grown following the RD route, and this prompted us to follow the growth from a structural point of view by means of XPD [32].

For this purpose, V depositions were performed at RT in an oxygen partial pressure of 5×10^{-8} mbar, with a deposition rate of 1.2 ± 0.2 Å min^{-1}. The growth parameters were optimized in order to reproduce as closely as possible literature electronic structure data for a layer grown in an analogous way [34, 35]. Once this requirement was met, a full 2π XPD characterization of the overlayers was performed as a function of thickness, up to approximately 20 ML. Figure 3 shows the Ti $2p_{3/2}$ and O 1s 2π patterns from clean, stoichiometric and ordered $TiO_2(110)$ and the V 2p and O 1s plots from a vanadia ultrathin film approximately 5 ML thick deposited at room temperature in an oxygen atmosphere. If the patterns obtained from the ultrathin films are compared with those measured on the clean substrate, the strong similarity appears immediately evident. The isomorphism of the patterns is preserved for layers as thick as ∼20 ML, although the anisotropy is strongly attenuated by a growing degree of structural

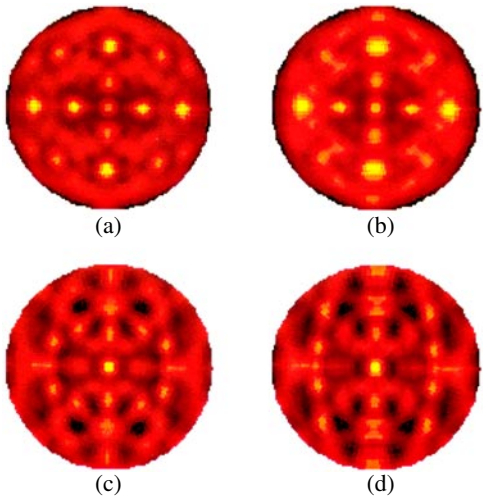

Figure 3. (*a*) Ti $2p_{3/2}$ and (*c*) O 1s 2π patterns from clean, stoichiometric and ordered $TiO_2(110)$; (*b*) and (*d*) V 2p and O 1s 2π plots from a vanadia ultrathin film ∼5 ML thick deposited at room temperature in 5×10^{-8} mbar O_2. The horizontal radius of each plot corresponds to the [001] main azimuth on the substrate surface.

disorder. However, a rather brief annealing at 473 K is sufficient to restore the local order in the thicker films at a level comparable to that of the 5 ML films. Hence, XPD data clearly show that vanadia ultrathin films grown on $TiO_2(110)$ by depositing V metal in an oxygen ambient at RT have a rutile crystal structure, and are therefore substantially different from layers grown in an analogous way on other crystalline substrates (e.g. $Al_2O_3(0001)$ [36] and Pd(111) [37]). It appears that $TiO_2(110)$, with its rutile structure, is particularly apt to stabilize the isomorphic vanadia phase. This finding could have profound consequences in our understanding of the particular catalytic properties of titania-supported vanadia catalysts, and it has been made possible only by the short-range order structural sensitivity of XPD.

3.2. Ultrathin oxide films and clusters from metalcarbonyl precursors

3.2.1. RuO_2 and Ru deposits on $TiO_2(110)$ from $Ru_3(CO)_{12}$ [38, 39]. Ruthenium and ruthenia/titania composites are interesting for a variety of fundamental and practical reasons. Ruthenium is known to be a catalyst for low-temperature methane coupling [40] and is active for CO and CO_2 methanation, particularly when it is partially oxidized on titania supports [41]. Ruthenia/titania mixed metal oxides are used in dimensionally stable anodes (DSAs). Mixed oxides are also used to chemically fine tune catalysts. Few studies on ruthenium and ruthenium oxide ultrathin films have appeared in the literature. The only studies available are on the epitaxial growth of RuO_2 on $TiO_2(110)$ [42] by molecular beam epitaxy (MBE) and the deposition of metallic Ru on graphite by e-beam evaporation [43]. The use of ruthenium carbonyls as alternative sources for the metal or oxide deposition has not yet been fully explored. A carbon-free metallic ruthenium overlayer was obtained by decomposing $Ru_3(CO)_{12}$ on Co(0001) [44] and Cu(111) in UHV [45].

In our study, we were able to obtain a clean decomposition of $Ru_3(CO)_{12}$ on a $TiO_2(110)$ surface, leading to the formation of ruthenium metallic particles that could be easily oxidized (10^{-6} mbar O_2 300 °C) to obtain ultrathin layers of epitaxial RuO_2.

Exposure of a clean and stoichiometric $TiO_2(110)$ surface to $Ru_3(CO)_{12}$ vapours (0.3 l) at room temperature—with no oxygen—led to a saturated surface where metallic Ru forms small disordered clusters, as demonstrated by XPS, XPD, STM, IRAS and TPD measurements [46].

On the other hand, the possibility of growing ruthenium oxide ultrathin films by oxidation of the metal deposit was demonstrated by heating the sample to 573 K in an O_2 atmosphere

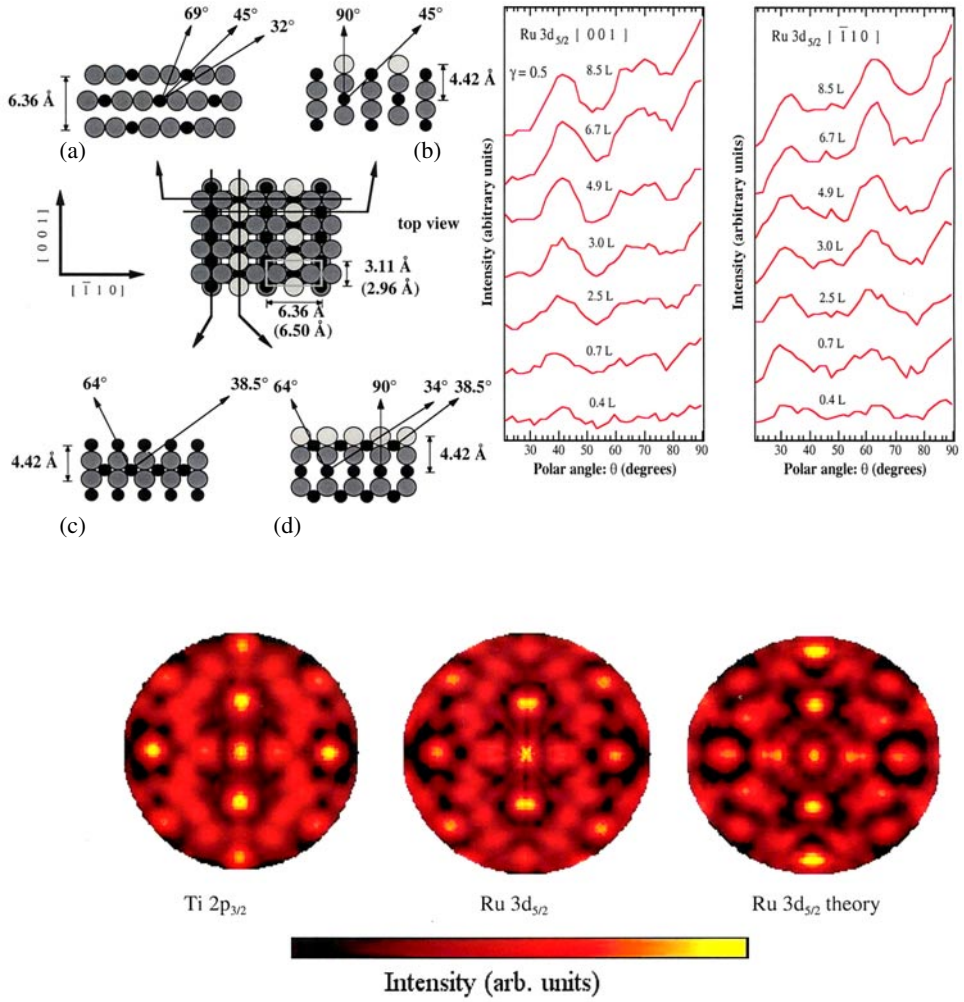

Figure 4. Left: the rutile(110) surface. Side views marked with (*a*) and (*b*) are aligned with the [$\bar{1}$10] direction, whereas (*c*) and (*d*) are aligned with the [001] direction. The unit cell sizes for the TiO_2 lattice are in parentheses. Small black circles represent metal atoms (Ti or Ru); large ones represent the oxygen atoms. The lighter shading indicates surface bridging oxygen atoms. Right: Ru $3d_{5/2}$ polar scans along [001] and [$\bar{1}$10] azimuths for RuO_2–TiO_2(110) ultrathin films obtained by annealing in O_2 (2×10^{-6} mbar) at 300 °C the deposits obtained by progressively increasing the dose of $Ru_3(CO)_{12}$. The lower part of the figure shows theTi $2p_{3/2}$ 2π plot ($E_k = 1027$ eV) from clean TiO_2(110), Ru $3d_{5/2}$ ($E_k = 972.6$ eV) from epitaxial RuO_2/TiO_2 and the best-fit theoretical Ru $3d_{5/2}$ 2π plot for relaxed RuO_2(110) (polar angles range from 90° to 10°).

(2×10^{-6} mbar) with a total exposure of 120 L. This treatment caused a shift of the Ru $3d_{5/2}$ peak from 280.1 eV (FWHM = 1.5 eV) to 281.5 eV (FWHM = 1.9 eV)—thereby demonstrating that the oxygen treatment oxidizes metallic Ru clusters to Ru oxide. By collecting XPD polar scans, along the [$\bar{1}$10] and [001] azimuths of the TiO_2 substrate, it was possible to demonstrate that the overlayer is indeed oxidized to form small RuO_2 clusters that grow epitaxially on the substrate surface. The Ru $3d_{5/2}$ XPD polar scans of samples annealed in oxygen for increasing precursor doses along [$\bar{1}$10] and [001] azimuths of the TiO_2 substrate are reported in figure 4 (top right). They show weak intensity maxima, which are nevertheless reproducible

and growing with the precursor dose, at about $\theta = 40^\circ$, 65° and 90°, and $\theta = 30^\circ$, 65° and 90°, respectively, for the two azimuths. The diffraction features obtained from the Ru $3d_{5/2}$ emission are very similar to those obtained for the Ti $2p_{3/2}$ line, as expected if the epitaxial RuO_2 clusters maintain the rutile lattice structure which characterizes both bulk RuO_2 and the TiO_2 substrates. From a quick look at the rutile structure, it is easy to evaluate the polar angles for which strong FS peaks are expected along the $[\bar{1}10]$ and [001] azimuths. In figure 4 (top left), side views of the rutile (110) structure aligned with the $[\bar{1}10]$ and [001] directions are reported, and the arrows indicate the main FS directions corresponding to metal atom emission. The presence of the above-mentioned diffraction peaks can be interpreted by assuming that the RuO_2 deposit grows by forming small three-dimensional $RuO_2(110)$ islands on the TiO_2 surface. In the case of a RuO_2 lattice, a polar scan recorded along the $[\bar{1}10]$ azimuth should present FS peaks at $\theta = 32^\circ$, 45° and 69°. Such FS events can be obtained if two layers both containing the metal and the oxygen ions are present (see the figure) and a minimum thickness of 4.42 Å is necessary. The peak at $\theta = 40^\circ$ seen in the polar curves along the [001] azimuth corresponds to one of the Ru–O bond directions and also to the bond directions of the bridging oxygen atoms on the surface. At least two layers containing the metal ions are necessary to originate the FS peak at about 65° (Ru–Ru) in the scans along azimuth [001], which corresponds to a minimum thickness of 4.42 Å, assuming a bridging-oxygen-terminated surface. Finally, the same thickness is also necessary in order to have a Ru–O FS peak at $\theta = 90^\circ$ for both $[\bar{1}10]$ and [001] azimuths. In conclusion, the presence of these peaks even from the very early stages of the deposition is a strong evidence of a cluster-like growth mode.

Good-quality ultrathin epitaxial films can also be easily obtained by decomposing the metalcarbonyl precursor in an O_2 atmosphere. A very sharp (1×1) LEED pattern was obtained by performing a reactive exposure to the carbonyl precursor (50 min, 300 °C 2×10^{-6} mbar O_2). From this surface it was possible to a acquire full-hemisphere 2π angular distributions for the Ru $3d_{3/2}$ feature that are compared with the corresponding 2π plot obtained from a clean $TiO_2(110)$ surface in figure 4 (bottom). The Ru $3d_{5/2}$ photoelectron diffraction data were analysed by means of multiple-scattering calculations. The best fit to the experimental data, reported in figure 4, was obtained by vertically relaxing the $RuO_2(110)$ surface and assuming a pseudomorphic growth on the $TiO_2(110)$ substrate. As in clean TiO_2, a buckling of sixfold- and fivefold-coordinated cations in the first layer was found, associated with a downward relaxation of bridging oxygens. The buckling of ruthenium atoms was found in the second layer, and an overall contraction of the distance between the topmost and the underlying cation bilayer was also detected.

3.2.2. MnO epitaxial nanoclusters on Pt(111) from $Mn_2(CO)_{10}$ [47, 48]. There were two main reasons to try to prepare MnO epitaxial ultrathin films and nanoclusters. The first one is related to the fact that the surface science of MnO has not been widely explored due to the difficulties in obtaining a reliable method for preparing a clean and stoichiometric surface. To this purpose it is worth recalling that MnO is an insulating oxide and charging effects are strongly present when using bulk crystals. The second reason is connected to the possibility of obtaining a cluster-like growth of MnO, which is a necessary condition to have supported oxide nanoparticles. A recent theoretical study predicts that nanoparticles of MnO would have ferromagnetic behaviour, while the bulk material undergoes a first-order paramagnetic to antiferromagnetic transition at 118 K [49].

The use of a metalcarbonyl precursor such as $Mn_2(CO)_{10}$ can be a very convenient approach to this task. $Mn_2(CO)_{10}$ does not adsorb on a Pt(111) surface at room temperature, while a reactive exposure of the Pt surface in a water atmosphere (8×10^{-7} mbar) at 200 °C to vapours of $Mn_2(CO)_{10}$ causes the precursor decomposition which leads to MnO. The XPS

data fully confirm the formation of MnO according to the position and line shape of the Mn 2p. XPS data also confirm the presence of zerovalent Mn in the early stages of deposition but—as soon as the exposures times increase—the Mn^0 component disappears and the Mn/O ratio reaches the stoichiometric value. Although the XPS data are indicative of the presence of a MnO deposit, a complete and unambiguous characterization can only be obtained from a surface structure determination of the film. Figure 5 (top left) reports azimuthal scans of the Mn 2p and O 1s regions recorded at $\theta = 55^\circ$ after a 30 min exposure. It is immediately evident that the deposit is characterized by a threefold symmetry axis (C_3), as expected for a NaCl-type structure grown along the [111] direction. Moreover, Mn 2p and O 1s azimuthal curves are similar to each other, which is an indication of the equivalence of the Mn and O crystal sites. In the same figure the corresponding scan for the Pt $4f_{7/2}$ region is reported, as a reference for the symmetry of growth. The three intense FS peaks corresponding to the Pt–Pt atomic rows allow one to identify the $\langle 1\bar{2}1\rangle$ azimuth, while the $\langle \bar{1}\bar{1}2\rangle$ directions are shifted by 60° and correspond to the less intense features of the curve. XPD polar scans were also acquired along the $[\bar{1}\bar{1}2]$ azimuth after each exposure to $Mn_2(CO)_{10}$ and H_2O. The intensity modulations of the curves, reported in figure 5 (bottom), can be easily assigned on the basis of a simple geometrical model that is useful in order to identify the main FS directions. Figure 5 (right) shows a side view of MnO layers grown along the [111] direction. The arrows indicate the main FS directions, assuming the Mn atom as the emitter. The O–Mn bond direction is found at $\theta = 35^\circ$, while the O–O (or Mn–Mn) FS directions are $\theta = 55^\circ$. These two directions are azimuthally shifted by $\Delta\phi = 60^\circ$. The polar scans show an intense peak at ca. $\theta = 55^\circ$, which increases in intensity with the exposure time, and a peak at $\theta = 90^\circ$, which is already present at low exposures. The presence of the peaks at $\theta = 90^\circ$ from the earlier deposit could be taken as an indication of a cluster-like growth, since at least four layers (two double layers containing the Mn–O bond) must be present in order to have a FS peak at $\theta = 90^\circ$. Two and three layers are sufficient to have FS diffraction features at $\theta = 35^\circ$ and 55°, respectively.

In a further experiment an RD to $Mn_2(CO)_{10}$ vapours led to a complete coverage of the substrate with a thickness of ca. 13 Å. The film showed a LEED (1×1) pattern ($E = 80$ eV) that was different from the Pt(111) substrate one. The surface lattice dimensions obtained (3.1 Å) are compatible with the bulk lattice parameter of a MnO(111) surface (3.14 Å). In figure 6 the O 1s and Mn 2p 2π XPD plots obtained for a freshly grown MnO surface are shown. The 2π plots are reported as χ functions, with $\chi = (I - I_0)/I_0$ where I is the absolute intensity of the diffraction pattern and I_0 is a smooth background obtained by a polynomial fitting of the azimuthal average of I. The Mn 2p and O 1s 2π plots were analysed by means of MS–SW simulations in order to obtain quantitative information on the surface structure. The best agreement with the experiment was found for a vertically relaxed MnO(111) surface with a surface unit cell vector $a = 3.14$ Å. The best fit (reported in figure 6) was always obtained in the case of O-terminated surfaces. This contraction could be easily inferred since the Mn–O FS peak was found at $\theta = 32^\circ$, while 35° should be expected for a bulklike MnO termination. This behaviour is also expected on the basis of the consideration that a (111) NaCl-type surface is a polar surface, for which a bulk termination should be energetically highly unfavourable, and by comparison with other experimental and theoretical findings in similar systems [50–52]. In the simulations the interlayer spacing of the outermost double layer was systematically varied, looking for the best fit with the experimental data. The interlayer spacing between the first O and Mn layers is thus decreased by ca. 0.3 Å and the spacing between layer 2 and layer 3 is decreased by ca. 0.2 Å. The calculated best-fit R-factors are 0.32 and 0.29 for Mn 2p and O 1s emission, respectively. The decrease in the interlayer spacing corresponds to a Mn–O bond distance, within the first two double layers, of 2.04 and 2.12 Å, compared with a bulk value of 2.220 Å. These values are compatible with the bond contractions found in the literature in the

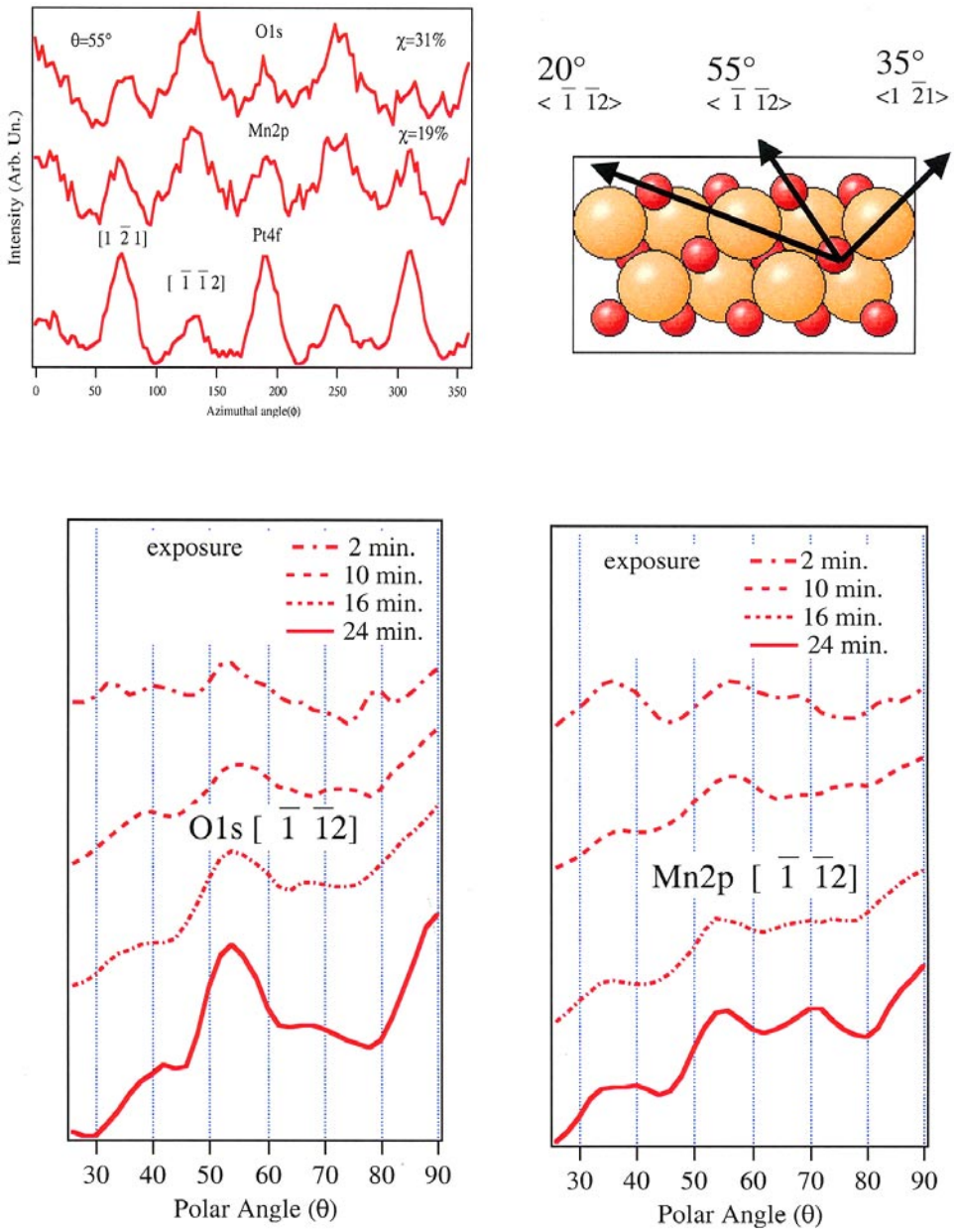

Figure 5. Al Kα excited Mn $2p_{3/2}$ and O 1s XPD azimuthal scans recorded after 30 min of reactive exposure of $Mn_2(CO)_{10}$ on Pt(111) in the presence of water (8×10^{-7} mbar). The Pt $4f_{7/2}$ azimuthal scan is reported as a reference. In the right-hand part of the figure a side view of the MnO(111) surface is reported together with the main forward-scattering directions indicated by the arrows. The lower portion of the figure shows Mn $2p_{3/2}$ and O 1s polar scans recorded along the [$\bar{1}\bar{1}$2] azimuthal direction and acquired after different exposure times to $Mn_2(CO)_{10}$ vapours.

case of CoO, where according to LEED measurements the Co–O bond distance at the surface is 2.09 Å [50], the bulk distance being 2.206 Å, and FeO grown on Pt(111), where the bond lengths found in the first two double layers were 1.9 and 2.1 Å, while the bulk value is 2.16 Å [51].

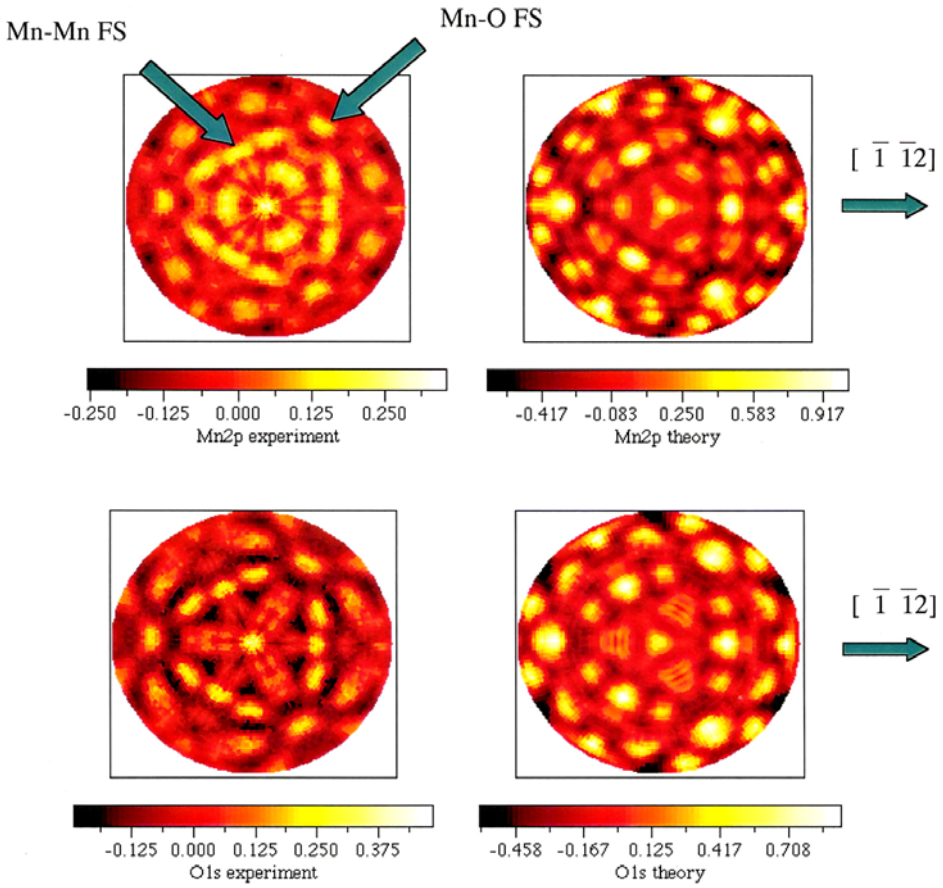

Figure 6. Al Kα excited Mn $2p_{3/2}$ and O 1s XPD 2π plots recorded after 30 min of reactive exposure of $Mn_2(CO)_{10}$ on Pt(111) in the presence of water (8×10^{-7} mbar). The polar angle ranges from 90° (centre of the plot) to 10° from the surface. Best-fit theoretical simulations are also reported.

4. Conclusions and perspectives

This brief overview has been focused on those aspects of ultrathin epitaxial oxide growth that are most conveniently investigated by means of angle-scanned XPD. It has been shown how XPD can give detailed and rather direct structural information on short-range-ordered epitaxial systems which is hardly accessible by means of other surface structural techniques. The merit of the technique is even more evident if the chemical specificity of XPD is additionally taken into account. Such information concerns site symmetries and occupancy, bond directions, lattice packing, the presence of epitaxial strain etc. Quantitative structural information (i.e. bond lengths) can additionally be extracted from experimental data if these are compared with theoretical single- or multiple-scattering cluster-based simulations of XPD patterns obtained from models of the system under investigation. Parameters are varied in a reasonable range and the best-fit structure is obtained via an *R*-factor analysis. A simple laboratory set-up composed by an x-ray source, an electron analyser and a sample manipulator capable of azimuthal and polar rotations in an UHV environment thus constitutes a powerful tool for the structural

investigation of locally ordered epitaxial systems, which has become a valuable aid in many surface and materials science laboratories around the world.

New developments in the field of photoelectron diffraction applied to surface and thin-film structures are mainly related to the use of synchrotron radiation. One of the fields where an important breakthrough has been recently achieved is photoelectron holography. After Gabor's concepts of holographic reconstructions of three-dimensional images from diffraction patterns [53] were applied to electron diffraction by Szöke [54], it was soon recognized that Fourier-transformed 2π XPD plots represent holograms of the atoms neighbouring the emitting species in the surface region of a locally ordered sample [55]. However, due to the anisotropic nature of electron–atom scattering in both phase and amplitude, the images resulting from the holographic reconstructions of 2π plots acquired in conventional geometries are heavily distorted. In this context, FS (which is a zeroth-order diffraction effect and thus contains no holographic information) is the main source of the problem. It has been recently proposed [56] that the acquisition of diffraction patterns from s levels, in an experimental arrangement such that the emitted intensity is detected near the nodal plane of the outgoing p primary wave, effectively suppresses FS, thereby strongly improving the quality of holographic reconstructions. The technique has been named near-node photoelectron holography. The feasibility of such an experiment has been successfully demonstrated at the beamline ALOISA at the ELETTRA synchrotron (Trieste, Italy), where three-dimensional images of atomic sites in the surface region of Al(111) have been obtained by relying on Al 2s emission [57]. The resolution of the holographic reconstruction is such that nearest, next-nearest and second-next-nearest neighbours of the emitter are clearly seen. The technique opens up unprecedented possibilities regarding direct, chemically specific three-dimensional imaging of supported molecules, clusters and thin films.

Another non-conventional implementation of XPD, recently proposed by our group [58] and confirmed experimentally at ALOISA [59], is variable-polarization photoelectron diffraction. This technique also exploits the anisotropic nature of the primary wave in s initial-state photoelectron emission, coupled to the degrees of freedom of the ALOISA beamline in setting up the relative orientation of the x-ray polarization vector, the sample normal and the direction of detection. In this case, two 2π plots in two distinct geometries are measured and their normalized ratio is compared with suitable theoretical simulations. It has been demonstrated that this ratio is extremely sensitive to surface relaxation, with an accuracy comparable to that of surface x-ray diffraction, but being additionally sensitive to short-range order and chemically specific. The technique has been applied successfully to the determination of TiO_2(110) [59] and ZnO(0001) [60] surface relaxation. In perspective, it could be a valuable tool in discerning between the homogeneous tensile or compressive strain versus the surface-energy-induced modifications of the topmost layers in short-range-ordered epitaxial clusters and/or thin films.

Acknowledgments

This work has been partially funded by 'Progetto Finalizzato Materiali Speciali per Tecnologie Avanzate II' of the CNR, Rome and by Ministero della Ricerca Scientifica e Tecnologica (MURST) through the national programme 'Strati ultrasottili di ossidi e solfuri inorganici: crescita, caratterizzazione e reattività superficiale'.

References

[1] Fork D K, Phillips J M, Ramesh R and Wolf R M 1994 *Epitaxial Oxide Thin Films and Heterostructures: Proc. Symp.* vol 341 (Pittsburgh, PA: Materials Research Society)

[2] Schlom D G, Eom Ch-B, Hawley M E, Foster Ch M and Speck J S 1997 *Epitaxial Oxide Thin Films III Proc. Symp.* vol 474 (Pittsburgh, PA: Materials Research Society)
[3] Henrich V E and Cox P A 1994 *The Surface Science of Metal Oxides* (Cambridge: Cambridge University Press)
[4] Bäumer M and Freund H-J 1999 *Prog. Surf. Sci.* **61** 127
Chambers S A 2000 *Surf. Sci. Rep.* **39** 105
[5] Fadley C S 1984 *Prog. Surf. Sci.* **16** 275
[6] Fadley C S 1987 *Phys. Scr.* T **17** 39
[7] Fadley C S 1992 *Synchrotron Radiation Research: Advances in Surface Science* ed R Z Bachrach (New York: Plenum)
[8] Fadley C S 1993 *Surf. Sci. Rep.* **19** 231
[9] Chambers S A 1990 *Adv. Phys.* **40** 357
[10] Chambers S A 1992 *Surf. Sci. Rep.* **16** 261
Egelhoff W F Jr 1990 *Crit. Rev. Solid State Mater. Sci.* **16** 213
[11] Granozzi G and Sambi M 1996 *Adv. Mater.* **8** 315
[12] Egelhoff W F Jr 1994 *Ultrathin Magnetic Structures I, an Introduction to Electronic, Magnetic and Structural Properties* ed J A C Bland and B Heinrich (Berlin: Springer)
[13] Kodas T T and Hampden-Smith J M 1994 *The Chemistry of Metal CVD* (Weinheim: VCH)
[14] Woodruff D P 1994 *Surf. Sci.* **299/300** 183
[15] Sambi M, Della Negra M, Granozzi G, Li Z S, Hoffmann Jørgensen J and Møller P J 1999 *Appl. Surf. Sci.* **142** 146
[16] Osterwalder J, Greber T, Wetli E, Wider J and Neff H J 2000 *Prog. Surf. Sci.* **64** 65 and references therein
[17] Chen Y and Van Hove M A web page http://electron.lbl.gov/mscdpack/
[18] Van Hove M A, Tong S Y and Elconin M H 1977 *Surf. Sci.* **64** 85
[19] Pendry J B 1980 *J. Phys. C: Solid State Phys.* **13** 937
[20] Li-Qiong Wang, Schach von Wittenau A E, Ji Z G, Wang L S, Huang Z Q and Shirley D A 1991 *Phys. Rev.* B **44** 1292
[21] Saiki S R S, Kaduwela A P, Sagurton M, Osterwalder J, Friedman D J, Fadley C S and Brundle C R 1993 *Surf. Sci.* **282** 33
[22] Bradshaw A M and Woodruff D P 1995 *Application of Synchrotron Radiation* ed W Eberhardt (Berlin: Springer)
[23] Sambi M, Sangiovanni G, Granozzi G and Parmigiani F 1996 *Phys. Rev.* B **54** 13464
[24] Centi G, Pinelli D and Trifirò F 1990 *J. Mol. Catal.* **59** 221
[25] Martín C, Rives V, Sánchez-Escribano V, Busca G, Lorenzelli V and Ramis G 1991 *Surf. Sci.* **251/252** 825
[26] Topsøe N-Y 1991 *J. Catal.* **128** 499
[27] Sambi M, Pin E, Sangiovanni G, Zaratin L, Granozzi G and Parmigiani F 1996 *Surf. Sci.* **349** L169
[28] Sambi M, Sangiovanni G, Granozzi G and Parmigiani F 1997 *Phys. Rev.* B **55** 7850
[29] Møller P J, Li Z S, Egebjerg T, Sambi M and Granozzi G 1998 *Surf. Sci.* **402–4** 719
[30] Negra M D, Sambi M and Granozzi G 1999 *Surf. Sci.* **436** 227
[31] Negra M D, Sambi M and Granozzi G 2000 *Surf. Sci.* **461** 118
[32] Sambi M, Negra M D and Granozzi G 2000 *Surf. Sci.* L116
[33] Negra M D, Sambi M and Granozzi G *Surf. Sci.* at press
[34] Biener J, Bäumer M and Madix R J 1999 *Surf. Sci.* **432** 178
[35] Madix R J, Biener J, Bäumer M and Dinger A 1999 *Faraday Discuss.* **114** 85
[36] Guo Q, Kim D Y, Street S C and Goodman D W 1999 *J. Vac. Sci. Technol.* A **17** 1887
[37] Leisenberger F P, Surnev S, Vitali L, Ramsey M G and Netzer F P 1999 *J. Vac. Sci. Technol.* A **17** 1743
[38] Rizzi G A, Magrin A and Granozzi G 1999 *Surf. Sci.* **443** 277
[39] Rizzi G A, Sambi M, Magrin A and Granozzi G 2000 *Surf. Sci.* **454–6** 30
[40] Lenzsolomun P, Wu M C and Goodman D W 1994 *Catal. Lett.* **25** 75
[41] Thampi K R, Kiwi J and Gratzel M 1987 *Nature* **327** 506
[42] Kim Y J, Gao Y and Chambers S A 1997 *Appl. Surf. Sci.* **120** 250
[43] Steierl G, Pfandzelter R and Rau C 1994 *J. Appl. Phys.* **76** 6431
[44] Vaari J, Lahtinen J and Hautojärvi P 1996 *Surf Sci.* **346** 11
[45] Sham T K, Ohta T, Yokoyama T, Kitajima Y, Funabashi M, Kosugi N and Kuroda H 1988 *J. Chem. Phys.* **88** 475
[46] Meier D C, Rizzi G A, Granozzi G, Lai X and Goodman D W submitted
[47] Rizzi G A, Zanoni R, Di Siro S, Perriello L and Granozzi G 2000 *Surf. Sci.* **462** 187
[48] Rizzi G A, Petukhov M, Sambi M, Zanoni R, Perriello L and Granozzi G 2001 *Surf. Sci.* **482–5** 1474
[49] Bloch D, Hermann-Ronzaud D, Vettier C, Yelon W B and Alben R 1975 *Phys. Rev. Lett.* **35** 963
[50] Ignatiev A, Lee B W and Van Hove 1977 *Proc. 7th IVC–3rd ICSS (Vienna)* p 2435

[51] Ranke W, Ritter M and Weiss W 1999 *Phys. Rev.* B **60** 1527
[52] Hermansson K, Baudin M, Ensing B, Alfredsson M and Wojcik M 1998 *J. Chem. Phys.* **109** 7515
[53] Gabor D 1948 *Nature* **161** 777
[54] Szöke A 1986 *Short Wavelegth Coherent Radiation: Generation and Applications (AIP Conf. Proc. Vol. 147)* ed D T Atwood and J Boker (New York: AIP) pp 361–467
[55] Barton J J 1991 *Phys. Rev. Lett.* **67** 3106
[56] Greber T and Osterwalder J 1996 *Chem. Phys. Lett.* **256** 653
[57] Wider J, Baumberger F, Sambi M, Gotter R, Verdini A, Bruno F, Cvetko D, Morgante A, Greber T and Osterwalder J 2001 *Phys. Rev. Lett.* **86** 2337
[58] Sambi M and Granozzi G 1998 *Surf. Sci* **415** L1007
[59] Verdini A, Sambi M, Bruno F, Negra M D, Gotter R, Floreano L, Morgante A, Rizzi G A and Granozzi G 1999 *Surf. Rev. Lett.* **6** 1201
[60] Sambi M, Verdini A, Morgante A, Casarin M and Granozzi G in preparation